Two-dimensional Halide Pb-Perovskite–Double Perovskite Epitaxial Heterostructures

*Ajeet Singh[1,2], Biao Yuan[3], Md. Habibur Rahman[4], Hanjun Yang[1,5], Angana De[5], Jee Yung Park[1], Shuchen Zhang[1], Libai Huang[5], Arun Mannodi-Kanakkithodi[4], Timothy J. Pennycook[3], Letian Dou[1,5]**

[1]Davidson School of Chemical Engineering, Purdue University, West Lafayette, Indiana 47907, United States.

[2]Department of Chemistry, Indian Institute of Technology Delhi, New Delhi 110016, India.

[3]EMAT, University of Antwerp, Groenenborgerlaan 171, 2020 Antwerp, Belgium.

[4]School of Materials Engineering, Purdue University, West Lafayette, Indiana 47907, United States.

[5]Department of Chemistry, Purdue University, West Lafayette, Indiana 47907, United States.

**E-mail: dou10@purdue.edu (L.D.)*

Abstract

Epitaxial heterostructures of two-dimensional (2D) halide perovskites offer a new platform for studying intriguing structural, optical, and electronic properties. However, difficulties with stability of Pb- and Sn-based heterostructures have repeatedly slowed progress. Recently, Pb-free halide double perovskites are gaining a lot of attention due to their superior stability and greater chemical diversity, but they have not been successfully incorporated into epitaxial heterostructures for further investigation. Here, we report epitaxial core-shell heterostructures via growing Pb-free double perovskites (involving combinations of Ag(I)-Bi(III), Ag-Sb, Ag-In, Na-Bi, Na-Sb and Na-In) around Pb perovskite 2D crystals. Distinct from Pb-Pb and Pb-Sn perovskite heterostructures, growths of the Pb-free shell at 45° on (100) surface of the lead perovskite core are observed in all Pb-free cases. The in-depth structural analysis carried out with electron diffraction unequivocally demonstrates the growth of the Pb-free shell along the [110] direction of the Pb perovskite, which is likely due to the relatively lower surface energy of the (110) surface. Furthermore, an investigation of anionic interdiffusion across heterostructure interfaces under the influence of heat was carried out. Interestingly, halide anion diffusion in the Pb-free 2D perovskites is found to be significantly suppressed, as compared to Pb-based 2D perovskites. The great structural tunability and excellent stability of Pb-free perovskite heterostructures may find uses in electronic and optoelectronic devices in the near future.

Keywords: Layered lead halide perovskites, layered Pb-free double halide perovskites, epitaxial core-shell heterostructures, density functional theory, anion diffusion

Introduction

Semiconductor hybrid nanostructures are composed of two or more distinctive semiconductor components.[1,2] A great degree of control over the composition, relative configurations of nanostructures, crystal phases, exposed facets, and interfaces is possible with rationally developed epitaxially grown hybrid nanostructures.[1–3] Minimizing the interfacial energy of hybrid nanostructures is achieved by having a minimal lattice mismatch between the two crystals, which is the fundamental factor in realizing epitaxial growth.[1,3–7] The basis of contemporary electronics and optoelectronics is epitaxial heterostructures based on oxide perovskites and III-V, II-VI, and transition metal dichalcogenide semiconductors.[8–16] Solution-phase epitaxy technologies like colloidal synthesis and chemical reduction may epitaxially build a wide spectrum of hybrid nanostructures on a large scale and in high yield at cheap cost.[1,4,5,7,17–21] For uses like solution-processed solar cells, light-emitting diodes, detectors, and lasers, halide perovskites—an emerging family of tunable semiconductors with desirable properties—are appealing.[22–30] Since their crystal lattices are naturally soft, they can tolerate lattice mismatch better than other materials, making them attractive for use in heterostructure creation and semiconductor integration.[31,32] Among halide perovskites, the structural and compositional versatility of layered Pb-perovskite allows for their outstanding photoluminescence (PL) quantum yield, short carrier lifetime, and optoelectronic tunability.[23,33–39] Recently, we reported the synthesis of epitaxially grown lateral heterostructures of layered Pb-perovskite using a two-step substrate assisted evaporation method, studied the anion migration in hetero-halide lateral heterostructures and established the role of organic spacer cation in suppression of anion migration.[40,41] The heterostructures with mix halides have invited lot of interest since our reporting of lateral heterostructures.[42–45] Meanwhile, the layered Pb-free perovskite structural analogous of Pb-perovskite are also inviting lot of interest from materials scientists due to their higher stability and more structural diversity.[46–54] The layered Pb-free perovskite exhibit weak broad white light emission originating from self-trapped excitons (STE) and defects generally require dopants to introduce emission.[55–57] The inability to use fluorescence spectroscopy for studying anion migration due to the layered Pb-free perovskite's weak and broad STE and defect emission necessitates novel approaches. One way to investigate anion-migration in Pb-free perovskites, using the PL spectra of Pb perovskite as a probe, is to integrate these two into a heterostructures.

In this work we synthesized core-shell $(R)_2PbX_4$-$(R)_4M^IM^{III}X_8$ heterostructures using a two-step solution-phase synthesis method. Here R = Phenylethylammonium (PEA^+) or Bithiophenylethylammonium ($2T^+$), $M^I = Ag^+$ or Na^+, $M^{III} = Bi^{3+}$ or Sb^{3+} or In^{3+}, and X = Br or I. In these heterostructures, the layered Pb-perovskite is located in the core, while the layered Pb-free perovskite is located in the periphery and does not emit any observable light. The study of the effect of heat on these novel heterostructures shows that there is no anion migration in the layered Pb-free Ag-based Pb-free perovskites and establishes that the layered Pb-free perovskites are highly stable when compared to Pb-perovskites which undergo rapid anion migration under the effect of heat.[40,41] Complementary first principles simulations confirm the preferred perovskite surface orientations. This research demonstrates that layered Pb-free perovskites are more stable than layered Pb-perovskites because, in addition to rigid organic spacer cations such as $2T^+$, the careful selection of metal cations also inhibits the anion migration.

Result and Discussion

Since both the core Pb-perovskite and the shell Pb-free perovskite are widely investigated, and the core-shell $(PEA)_2PbBr_4$-$(PEA)_4AgBiBr_8$ heterostructure offers exceptional control on synthesis and reproducibility, it was chosen as a model system for investigations.[40,55] The organic spacer cation is same in both individual components and the size of organic spacer cation largely affects the inter-layer spacing between adjacent inorganic layers, so the lattice mismatch is low[51,58], and both core and shell perovskites were realized using similar solvent and anti-solvent combination as discussed in experimental section in SI. The $(PEA)_2PbBr_4$ was chosen as core as it is highly fluorescent and makes it easier to observe the changes in fluorescence in the heterostructure using an optical microscope. **Figure 1a** shows the schematic representation of the two-step synthesis of $(PEA)_2PbBr_4$-$(PEA)_4AgBiBr_8$ heterostructure microcrystals via substrate-assisted evaporation method.[40] The two-steps consists of the synthesis of pure $(PEA)_2PbBr_4$ followed by the growth of the shell of $(PEA)_4AgBiBr_8$. The boundary between the emitting core $(PEA)_2PbBr_4$ and non-emitting shell $(PEA)_4AgBiBr_8$ is easily identified using an optical microscope by comparing the bright-field image (BF image) with the corresponding PL image, as shown in **Figure 1b**. The bright purple emission from $(PEA)_2PbBr_4$ marks the interface with non-emissive $(PEA)_4AgBiBr_8$. The X-ray diffraction (XRD) profiles of pure $(PEA)_2PbBr_4$ and pure $(PEA)_4AgBiBr_8$ in **Figure 1c** match excellently with the respective reference XRD profiles, with equidistant peaks

corresponding to the [001] direction being observed.[48,59] The XRD profile of the $(PEA)_2PbBr_4$-$(PEA)_4AgBiBr_8$ heterostructure microcrystals also shows characteristic equidistant peaks along the [001] direction confirming no change in crystal structure occurs during the heterostructure synthesis. Interestingly the XRD pattern of the heterostructure does not show any peak corresponding to either pure $(PEA)_2PbBr_4$ or pure $(PEA)_4AgBiBr_8$, as can be seen in the enlarged view of the peaks corresponding to (001) and (002) planes, also, we did not observe any broadening of the peaks or splitting in the peaks.[40]

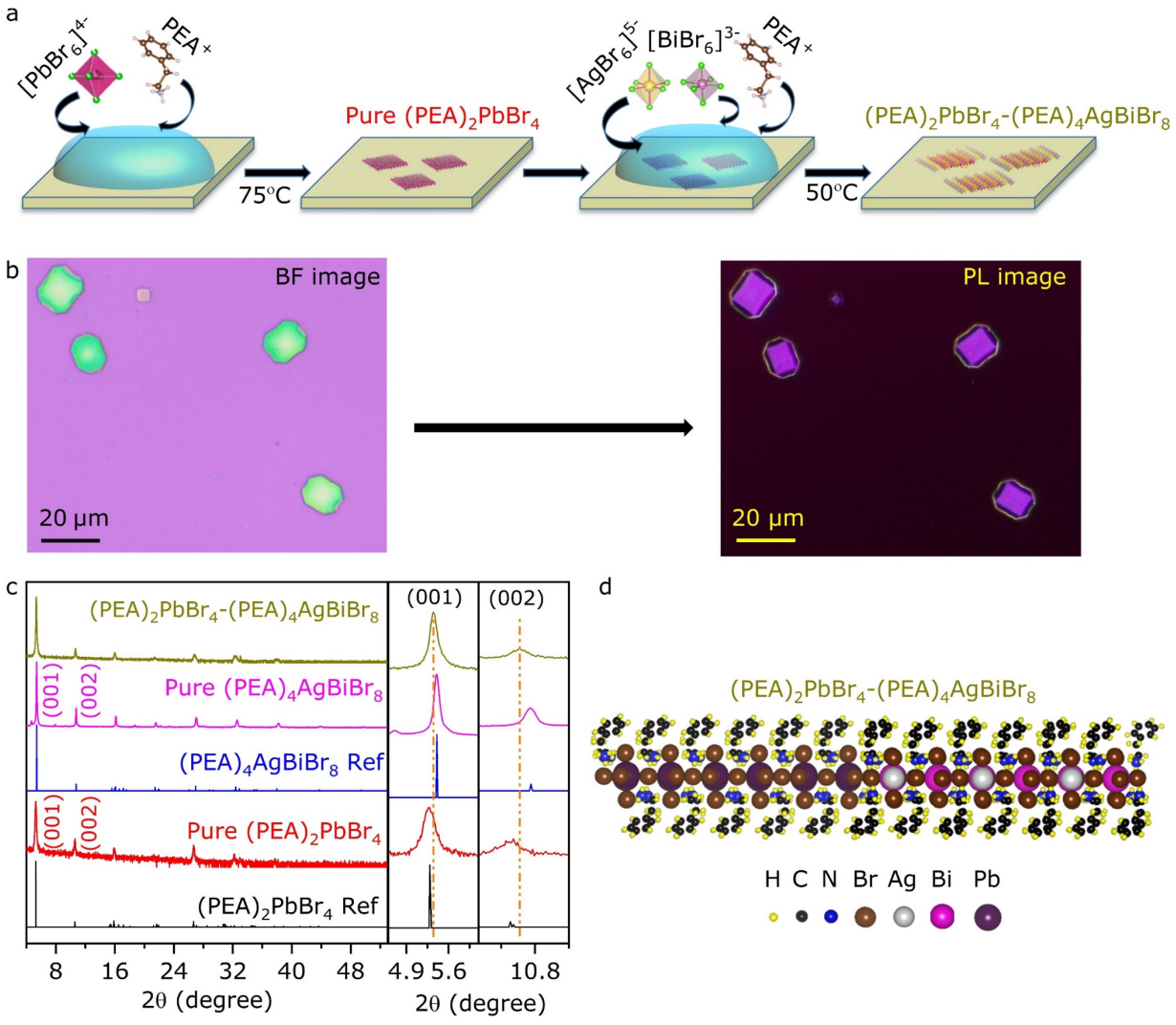

Figure 1. (a) The schematic representation of synthesis of $(PEA)_2PbBr_4$ and $(PEA)_2PbBr_4$ - $(PEA)_4AgBiBr_8$ HS microcrystals. **(b)** The bright-field (BF) and corresponding fluorescence (PL) image of $(PEA)_2PbBr_4$ -$(PEA)_4AgBiBr_8$ under white light excitation. **(c)** The XRD profiles of pure $(PEA)_2PbBr4$, pure $(PEA)_4AgBiBr_8$, respective reference XRD patterns[48,59], and $(PEA)_2PbBr_4$-$(PEA)_4AgBiBr_8$ HS microcrystals. (The orange dash-dot lines mark the position of heterostructure peaks for (001) and (002) planes) **(d)** Side view of crystal structure in $(PEA)_2PbBr_4$-$(PEA)_4AgBiBr_8$ HS along the [010] direction, generated using VESTA.[60]

The XRD profile of the heterostructure reveals that the lattice parameters of both constituent materials are altered during synthesis when compared with those of corresponding individual 2D perovskites. The heterostructure peaks corresponding to (001) planes when compared to pure core $(PEA)_2PbBr_4$ are shifted towards a higher 2θ, indicating the contraction of lattice planes with shell growth which is probably happening due to the pressure exerted by shell material. Whereas when compared to pure $(PEA)_4AgBiBr_8$, the peaks in heterostructure are shifted towards a lower 2θ, showing that the growth at the interface of $(PEA)_2PbBr_4$ also affects the lattice parameters of $(PEA)_4AgBiBr_8$, this might be occurring to minimize the lattice strain at the interface. The XRD profile analysis suggests that the alternating organic spacer-inorganic polyhedral layer arrangement offers unique flexibility in crystal structure. **Figure 1d** shows the side view of the crystal structure at the interface for pure $(PEA)_2PbBr_4$ and pure $(PEA)_2AgBiBr_8$ along [100] directions showing the similar arrangement of organic spacer cations resulting in a small lattice mismatch of 1.41% as calculated along (00l) from the individual structure parameters.[51,58,61] The core-shell morphology of heterostructure microcrystals was established using scanning electron microscope with energy dispersive X-ray spectroscopic elemental mapping (SEM-EDX) and atomic force microscopy (AFM). The SEM-EDX elemental mapping of $(PEA)_2PbBr_4$-$(PEA)_4AgBiBr_8$ heterostructures as shown in **Figure S1**. The elemental distribution of Ag over the entire surface of both heterostructure particles suggests that growth of Pb-free halide double perovskite happens in lateral as well as vertical directions. The Pb and Bi could not be distinguished using SEM-EDX due to the close value of Lα values (Pb Lα = 10.55 KeV and Bi Lα = 10.83 KeV).[62] The height profile of $(PEA)_2PbBr_4$ particles before and after heterostructure synthesis provided in **Figure S2** obtained using AFM confirms the core-shell morphology of

$(PEA)_2PbBr_4$-$(PEA)_4AgBiBr_8$ heterostructure. The height profile confirms the robust growth of the shell of $(PEA)_4AgBiBr_8$ in all directions: lateral and vertical, over the $(PEA)_2PbBr_4$ core.

The growth of the $(PEA)_4AgBiBr_8$ shell happens at 45° along the edge of the $(PEA)_2PbBr_4$ core as shown in **Figure S3**. We monitored the evolution of the morphology of the $(PEA)_2PbBr_4$-$(PEA)_4AgBiBr_8$ heterostructure with successive synthesis cycles of shell growth on the same piece of the core $(PEA)_2PbBr_4$ microcrystal using an optical microscope (by repeatedly taking the samples out of the reaction chamber for optical characterization and then putting back for next round of growth), as shown in **Figure 2a**. The growth is robust despite many perturbations. The shell grows into a square around a square at 45° continuously as observed in optical images. This unique epitaxial growth of the shell $(PEA)_4AgBiBr_8$ over the core $(PEA)_2PbBr_4$ in core-shell $(PEA)_2PbBr_4$-$(PEA)_4AgBiBr_8$ heterostructure microcrystals requires a deep understanding of the growth mechanism and crystal orientation at the interface. To understand the crystal orientation and epitaxial shell growth direction, the electron diffraction patterns were collected using transmission electron microscope (TEM). **Figure 2b** shows the TEM image of pure $(PEA)_2PbBr_4$ microcrystal with marked crystal orientation obtained from the analysis of the electron diffraction pattern provided in **Figure 2c**. We simulated the electron diffraction pattern using py4DSTEM for the pure $(PEA)_2PbBr_4$ and matched it with the experimental electron diffraction pattern to obtain the epitaxial direction as shown in **Figure S4**.[63] The electron diffraction pattern analysis confirms the orientation of epitaxial growth along the [l00] direction or [010] direction. **Figure 2d** shows the TEM image of the core-shell $(PEA)_2PbBr_4$-$(PEA)_4AgBiBr_8$ heterostructure microcrystal with the core marked by a white dashed rectangle. Very interestingly, the shell's growth direction appears to be parallel to the [110] direction, especially at 45°. To distinguish the core and shell, the PL image was also collected for the same microcrystal on top of TEM grid, see **Figure 2e** (inset provides BF image). The orange rectangle marks the edge of the fluorescent $(PEA)_2PbBr_4$ core. We collected selected area electron diffraction (SAED) patterns at different areas of the crystal. The electron diffraction collected from the center of the crystal will have contribution from both core $(PEA)_2PbBr_4$ and shell $(PEA)_4AgBiBr_8$ whereas the pattern from the corner will only have contribution from the shell $(PEA)_4AgBiBr_8$, thus providing us better insight into the crystal structure. The electron diffraction pattern of the core area and shell $(PEA)_4AgBiBr_8$ are similar in the location and intensity of the diffraction spots, see **Figure 2f and 2g**. The sharp diffraction spots also confirm the high crystallinity of the core and shell materials. The SAED pattern corresponding

to both the core and shell areas only shows one set of diffraction spots instead of split diffraction patterns as the in-plane lattice parameters a and b for $(PEA)_4AgBiBr_8$[51] are 11.5184 Å and 11.6000 Å and for $(PEA)_2PbBr_4$[58] are 11.6124 Å and 11.6388 Å. The in-plane lattice mismatch for a and b parameters in Pb-perovskite and Pb-free perovskite is 0.8% and 0.3%, respectively, resulting in the observation of same electron diffraction pattern at corner and center of the heterostructure particle. The in-plane lattice parameters in Pb-perovskite core and Pb-free perovskite shell are so close in value that these cannot be distinguished by the electron diffraction patterns as observed in **Figure 2f** and **2g**. This is further confirmed by the quantification of SAED spots. The position of the diffracted spots with respect to the transmitted spot show no change in d-spacing of in-plane lattice planes in the inorganic layer in **Figure 2f** and **2g** for core-shell heterostructure when compared to **Figure 2c** for pure $(PEA)_2PbBr_4$, suggesting that core-shell heterostructure formation does not affect the inorganic layer. To explain this, we hypothesize that the organic spacer cation layer in this alternate rigid-inorganic layer and flexible-organic layer arrangement in the layered halide perovskites provides flexibility of tuning of lattice parameters (corresponding to (00l) direction as observed from XRD patterns) to minimize strain, in otherwise highly crystalline materials.

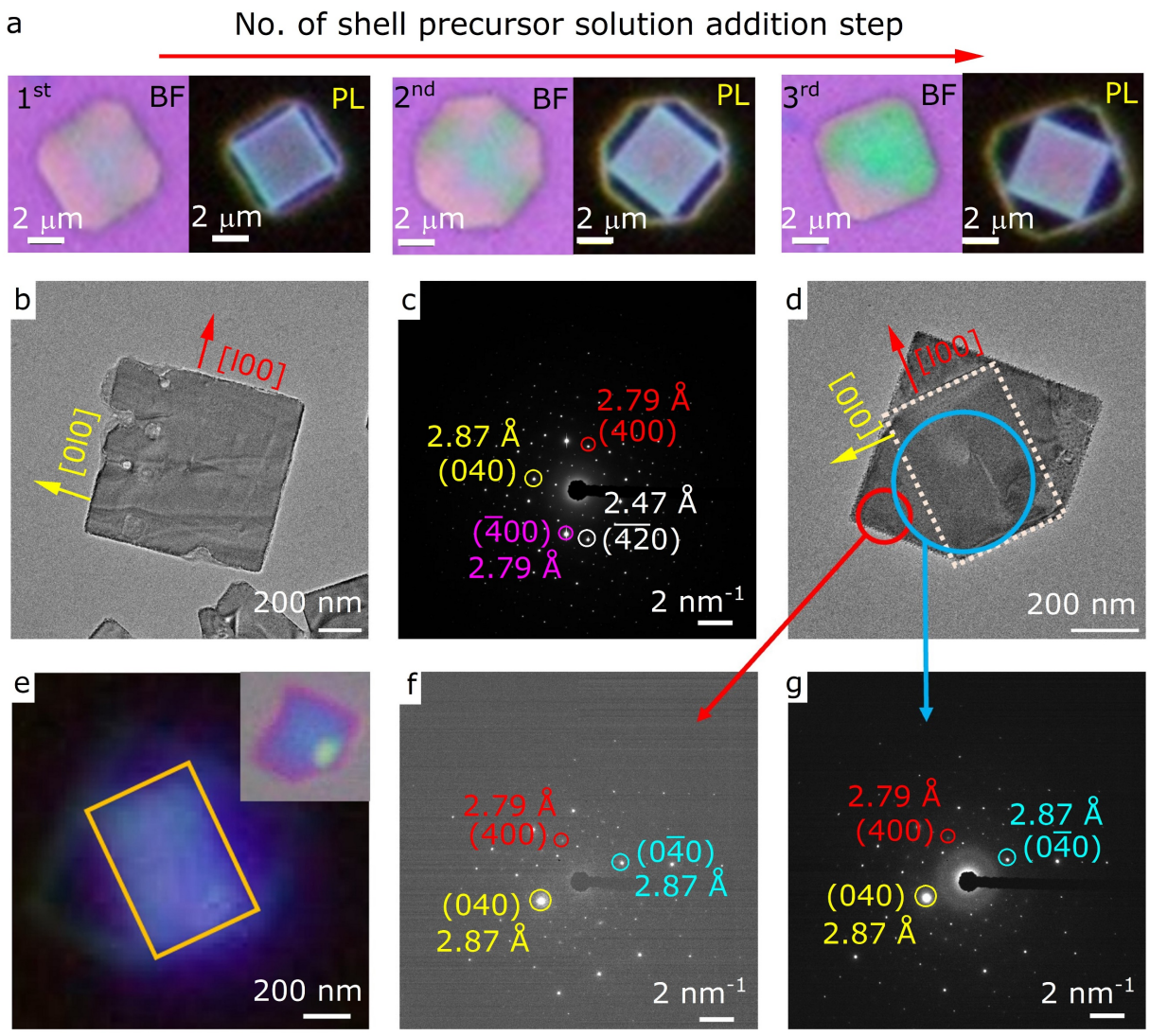

Figure 2. (a) The optical BF and corresponding PL images of $(PEA)_2PbBr_4$-$(PEA)_4AgBiBr_8$ heterostructure microcrystal with the number of times the shell precursor is added. **(b)** A TEM image showing the square morphology of pure $(PEA)_2PbBr_4$ crystal. **(c)** The corresponding diffraction pattern of **(b)**. **(d)** TEM image of $(PEA)_2PbBr_4$-$(PEA)_4AgBiBr_8$ heterostructure microcrystal. **(e)** corresponding PL image with BF image in inset. **(f)** and **(g)** selected area electron diffraction pattern corresponding to the epitaxial shell and core area, respectively.

To understand the thermodynamics of shell growth, we performed density functional theory (DFT) computations to determine the surface energy of the <100>, <110>, and <111> surfaces of $(PEA)_4AgBiBr_8$ and $(PEA)_2PbBr_4$. Interestingly, the <110> surface of $(PEA)_4AgBiBr_8$ can be

either Ag-octahedra terminated or Bi-octahedra terminated as shown in **Figure S5**, which results in different surface energies. DFT details and equations to compute the surface energy are included in the SI. **Figures 3a** and **3b** show the $(PEA)_4AgBiBr_8$ bulk crystal structure and Ag-terminated <110> surface slab respectively; the total DFT energies of both are utilized in determining the surface energy. **Figure 3c** shows the surface energy values obtained for various surfaces of $(PEA)_4AgBiBr_8$. We found that Bi-terminated <110> surface has the highest energy and the Ag-terminated <110> surface has the lowest surface energy, indicating that the growth of Ag-terminated surface is thermodynamically more feasible. Similarly, **Figures 3d** and **3e** respectively show the structures of bulk and <100> surface of $(PEA)_2PbBr_4$, used for surface energy calculations. **Figure 3f** shows the surface energy values obtained for three different surfaces of $(PEA)_2PbBr_4$. The <100> surface has the lowest surface energy and would thus be the most thermodynamically favorable growth direction. The comparison of surface energy values for various surfaces for Pb-crystal and Pb-free crystal provides critical insights into the growth of Pb-free perovskite shell at 45° from the exposed <100> surface of Pb-perovskite crystal. The 45° growth happens due to the growth of Pb-free crystal parallel to the [110] direction with Ag-terminated (110) plane growth being the determining factor as suggested by the surface energy computations.

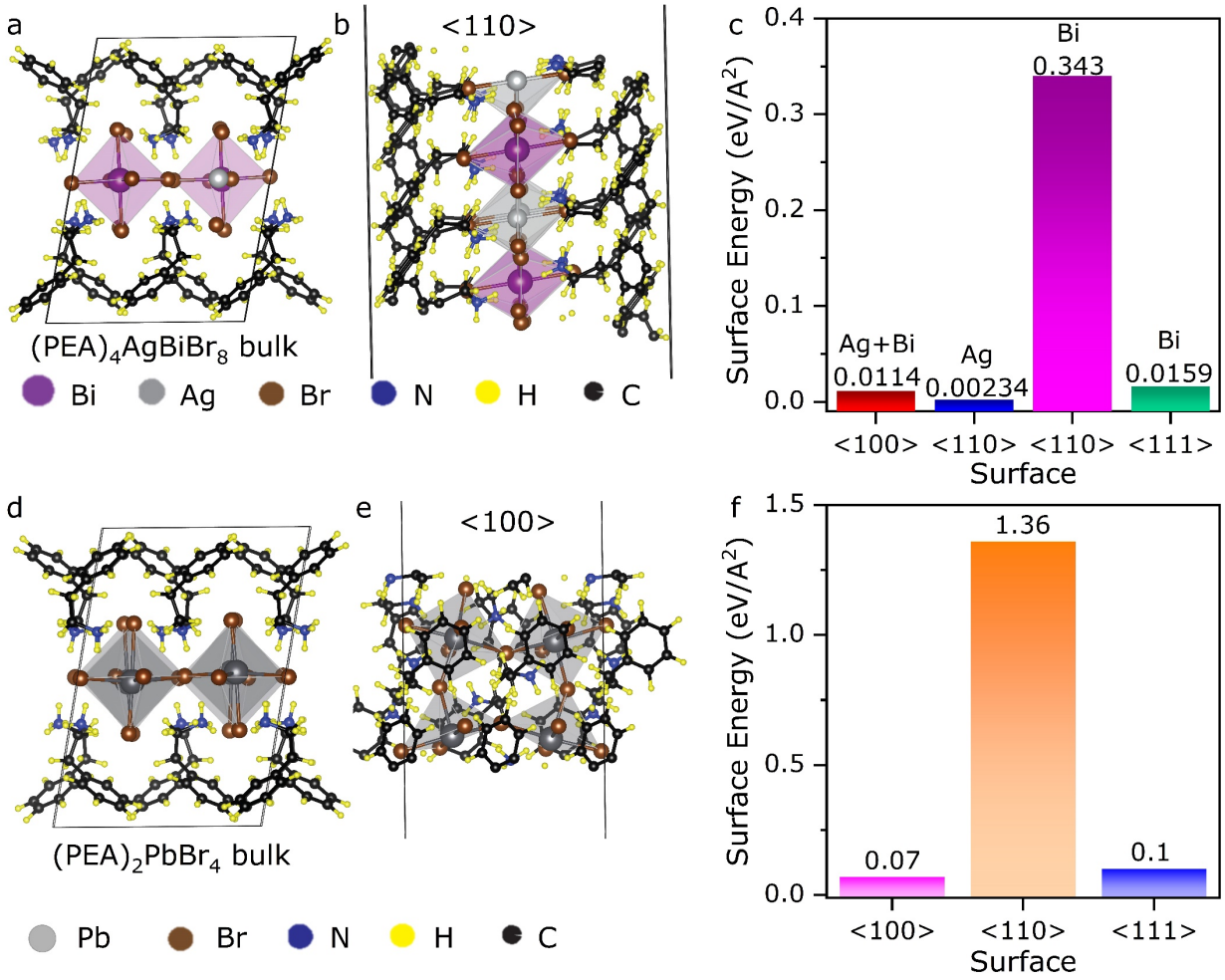

Figure 3. (a) Bulk $(PEA)_4AgBiBr_8$, **(b)** <110> surface of $(PEA)_4AgBiBr_8$, and **(c)** Surface energy values plotted for each surface: <100>, Ag-terminated <110>, Bi-terminated <110> and <111>. **(d)** Bulk $(PEA)_2PbBr_4$, **(e)** <100> surface of $(PEA)_2PbBr_4$, and **(f)** Surface energy values plotted for each surface: <100>, <110> and <111>. The boxes represent DFT simulation cells, and the grey/purple shaded regions represent perovskite octahedral units.

Optical properties of the core-shell heterostructures are observed to be comparable to that of free-standing core microcrystal. **Figure S6a** shows the steady-state absorption spectra of $(PEA)_2PbBr_4$, Pb-free $(PEA)_4AgBiBr_8$, $(PEA)_4AgSbBr_8$, and $(PEA)_4AgInBr_8$ with distinct excitonic peak centered around 395 nm, 425 nm, 411 nm, and 370 nm, respectively, and their core-shell heterostructures. From the absorption spectra the optical band gap follows the sequence Bi<Sb<Pb<<In similar to the values reported in the literature.[55] The PL spectra of $(PEA)_2PbBr_4$

and the core-shell $(PEA)_2PbBr_4$-$(PEA)_4AgBiBr_8$, $(PEA)_2PbBr_4$-$(PEA)_4AgSbBr_8$, $(PEA)_2PbBr_4$-$(PEA)_4AgInBr_8$ provided in **Figure S6b**, show a very sharp emission peak centered ~ 411 nm corresponding to excitonic emission from $(PEA)_2PbBr_4$ with insignificant shift of ~1 nm in case heterostructures.[40] A broad emission 490-620 nm arising due to the presence of self-trapped excitons (STE) is also observed with slight increase in emission intensity in heterostructures owing to the contribution from STE emission from the Pb-free perovskite shell.[55] The pure Pb-free PL spectra given in **Figure S6c** shows that the Pb-free perovskites have very weak broad white light.[55,56] The average lifetime values (see TableS2), obtained from fitting of the kinetics obtained using time-resolved PL (TRPL) show that the heterostructure formation does not affect the charge carrier dynamics observed at to 411 nm and broad STE emission 550 nm as given in **Figure S6d** and **S6e**, respectively. The unaffected absorption and PL spectra of $(PEA)_2PbBr_4$ in core-shell heterostructure can be justified by no observed change in in-plane lattice parameters of the inorganic layer i.e., the Pb-Br-Pb angles remain unchanged during heterostructure synthesis.

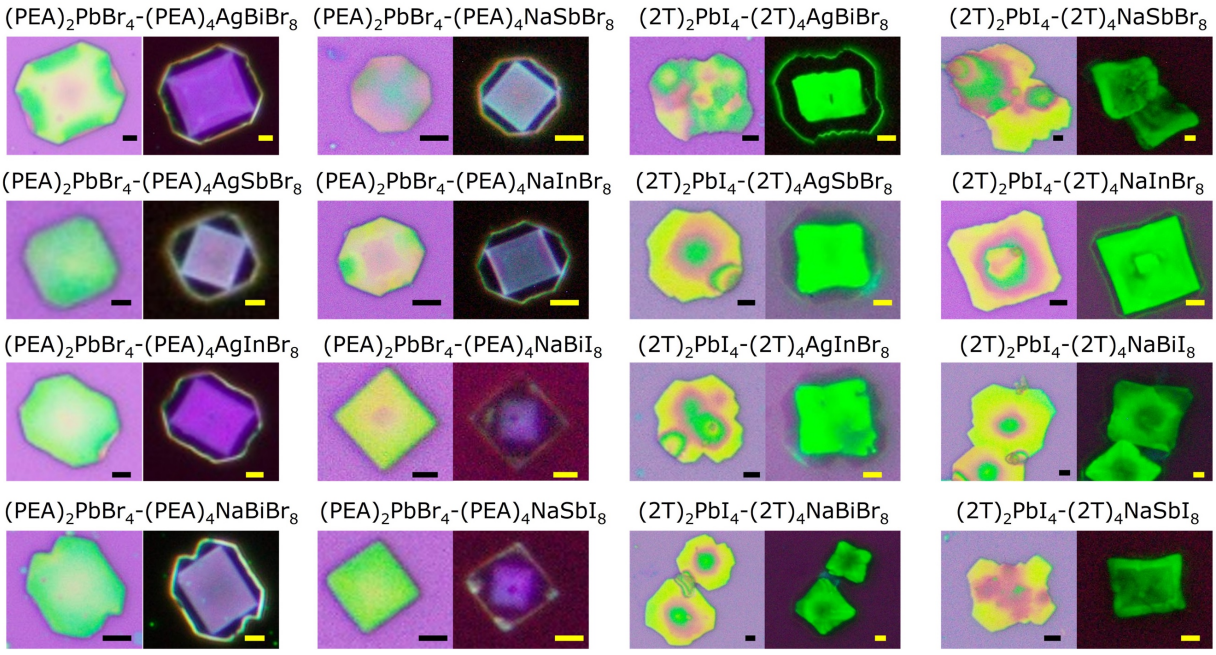

Figure 4. The BF images and corresponding PL images of various heterostructures we synthesized. Each BF and PL image pair is labelled. All the scale bars are 2 μm.

We demonstrate that the solution-based synthesis method can be expanded to double perovskites heterostructures involving silver and sodium as the M(I) cation, and Sb, Bi or In as the M(III) cation. We also prove that the chemical properties of the organic spacer showed little or no interference with the synthesis method, as shown by the success of both the PEA ligand as well as the thiophene-based 2T ligands, see **Figure S7** for ligand structure. Ultimately, complex heterostructures where both the halide and metal composition are simultaneously modified can be facially obtained, proving the robustness of the reported synthesis. **Figure 4** illustrates various synthesized heterostructures. Because $(PEA)_2PbI_4$ is unstable and fully dissolves during the synthesis process and $(2T)_2PbBr_4$ lacks fluorescence, it is difficult to identify the core from the shell. Hence, we solely focused on the synthesis of the heterostructures of $(PEA)_2PbBr_4$ and $(2T)_2PbI_4$.[40] **Figure S8** shows the PL emission of the as-synthesized pure $(2T)_2PbI_4$, pure Pb-free layered halide double perovskites, and various heterostructures. Similar to the PEA^+-based heterostructures, we did not observe any change in the PL spectra of $2T^+$-based heterostructures. The PXRD patterns of all the PEA^+ and $2T^+$-based heterostructures are provided in **Figure S9** and **S10**, respectively, the equidistant peaks corresponding to [001] direction confirmed the layered structures. We also did elemental mapping of the core-shell $(2T)_2PbI_4$-$(2T)_4AgBiBr_8$ heterostructure using SEM-EDX, provided in **Figure S11**. In case of the $(2T)_2PbI_4$-$(2T)_4AgBiBr_8$ heterostructure particle, the elemental distribution of I and Br shows that the I is confined to the core $(2T)_2PbI_4$ particle and Br is more concentrated in the lateral shell as indicated by the high intensity, and the low intensity of Br on top of core $(2T)_2PbI_4$ particle suggests the thinner vertical growth and thus inferring the formation of core-shell morphology. The $(PEA)_2PbBr_4$ and $(2T)_2PbI_4$ microcrystals are found to be very stable and work as excellent core material for realizing numerous core-shell heterostructures.

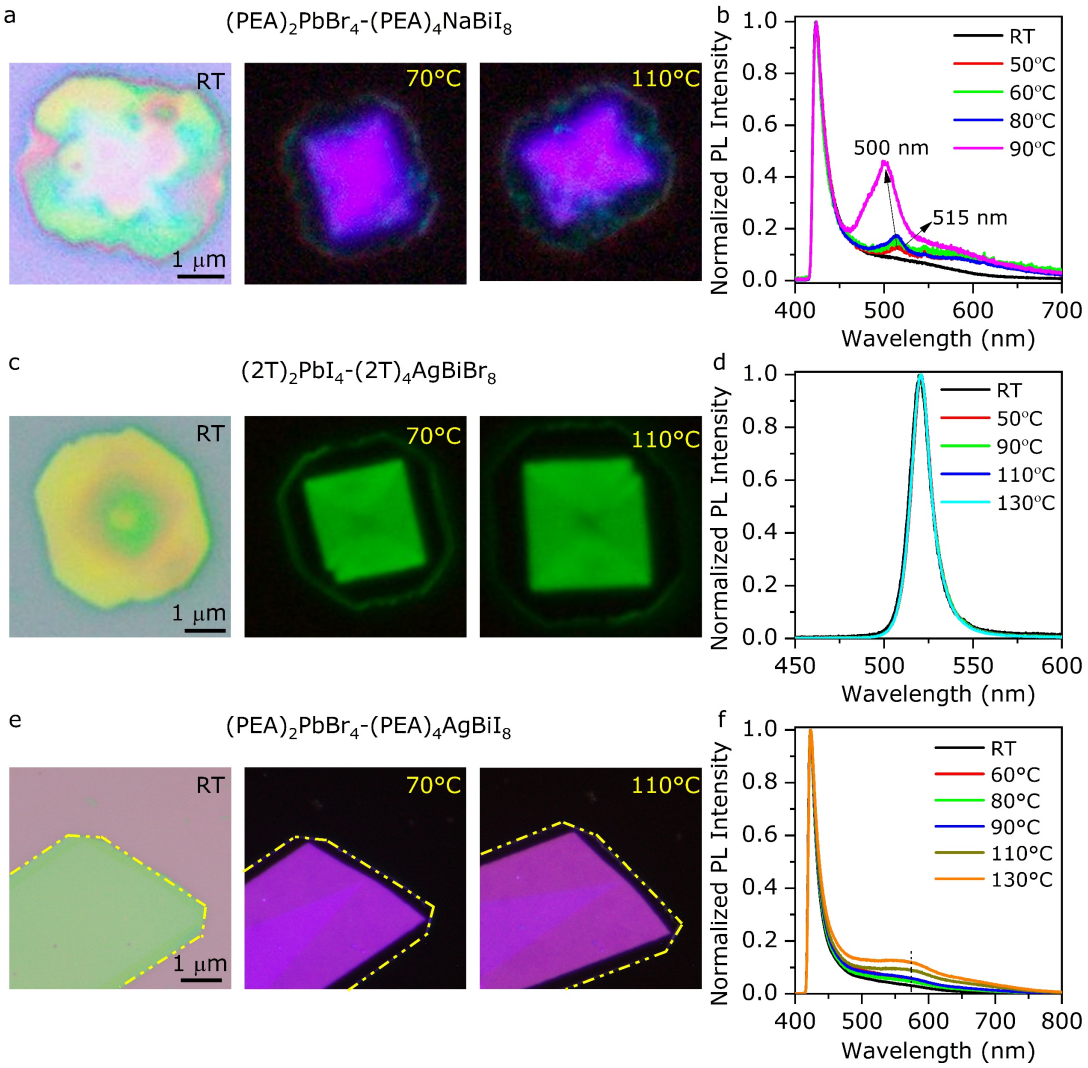

Figure 5. (a) The optical microscope BF and corresponding PL images of $(PEA)_2PbBr_4$-$(PEA)_4NaBiI_8$ heterostructure after heating at 70°C and 110°C for 30 min. **(b)** The PL spectra of the $(PEA)_2PbBr_4$-$(PEA)_4NaBiI_8$ heterostructure after heating at various temperatures. **(c)** The optical microscope BF and corresponding PL images of $(2T)_2PbI_4$-$(2T)_4AgBiBr_8$ heterostructure after heating at 70°C and 110°C for 30 min. **(d)** The PL spectra of the $(2T)_2PbI_4$-$(2T)_4AgBiBr_8$ heterostructure after heating at various temperatures. **(e)** The optical microscope BF and corresponding PL images of $(PEA)_2PbBr_4$-$(PEA)_4AgBiI_8$ heterostructure after heating at 70°C and 110°C for 30 min. **(f)** The PL spectra of the $(PEA)_2PbBr_4$-$(PEA)_4AgBiI_8$ heterostructure after heating at various temperatures.

In order to study the anion interdiffusion in Pb-free layered mix-halide perovskite heterostructures, the $(PEA)_2PbBr_4$-$(PEA)_4NaBiI_8$, $(PEA)_2PbBr_4$-$(PEA)_4AgBiI_8$, and $(2T)_2PbI_4$-$(2T)_4AgBiBr_8$ heterostructure microcrystals featuring different halide anions in the core and the shell were heated at increasing temperature at fixed time interval of 0.5 hours, presented in **Figure 5**. The optical microscope BF and PL images provided in **Figure 5a** show the PL images taken after heating the sample for 30 mins at 70°C and 110°C, the generation of faint green emission was observed after heating the sample at 110°C for 30 min. The $(PEA)_2PbBr_4$-$(PEA)_4NaBiI_8$ heterostructure emission spectra provided in **Figure 5b**, showed generation of a sharp new green emission feature originating from the inward migration of the iodine anions. The iodine anions migrate from the shell $(PEA)_4NaBiI_8$ into the core $(PEA)_2PbBr_4$ and gives rise to a mix halide $(PEA)_2Pb(Br_x/I_{1-x})_4$.[40,64,65] With increasing temperature the new feature continuously shifts from 515 nm towards 500 nm indicating the increased extent of migration of the iodide from the Pb-free shell into the lead-based core. Whereas the optical microscope images of the $(2T)_2PbI_4$-$(2T)_4AgBiBr_8$ heterostructures show no change and the corresponding PL spectra also do not show any shift or generation of new features as shown in **Figure 5c** and **5d**, suggesting that the rigid polythiophene ligand can suppress anion migration similar to the observed behavior earlier reported.[40] The **Figure 5e** and **5f** show the optical microscope images and PL spectra of $(PEA)_2PbBr_4$-$(PEA)_4AgBiI_8$ heterostructure, respectively, the PL images show no change after heating and similarly the PL spectra also showed no shift in the emission peak at 413 nm but the enhancement of the broad STE emission (500 nm – 650 nm) was observed. To understand this increment in STE emission intensity the pure $(PEA)_2PbBr_4$, pure $(PEA)_4AgBiI_8$, and $(PEA)_2PbBr_4$-$(PEA)_4AgBiBr_8$ heterostructure were heated at 80°C for an extended period of time and the PL spectra were monitored at various time intervals. **Figure S12a** shows the BF image and the PL images of the heterostructure particle after 10 min under white light and after 150 hours under white light and under laser light showed no trace of green emission and the PL spectra in **Figure S12b** show that there is no shift in emission at 413 nm, whereas the intensity of the broad STE emission increased with time. The absence of a sharp green emission and no shift in STE emission feature indicate the absence of anion migration in the $(PEA)_2PbBr_4$-$(PEA)_4AgBiBr_8$ heterostructure. The highly covalent nature of Ag-I bonding in comparison to more ionic Na-I bonding inhibits anion migration.[66] The observation hints at the importance of designing the Pb-free perovskites composition to minimize the anion migration in Pb-free perovskites and Pb-perovskites in device

design. The pure $(PEA)_2PbBr_4$ showed very little increase in STE emission whereas we observed significant increment in STE emission from $(PEA)_4AgBiI_8$ within 48 hours as can be seen in **Figure S12c** and **S12d**, respectively.[57] This increment in STE emission intensity in core $(PEA)_2PbBr_4$ and shell $(PEA)_4AgBiI_8$ results in the increased STE emission intensity, owing to the thermal annealing in the heterostructure after heating.

Conclusion

In summary, we have demonstrated the integration of Pb-free perovskites with Pb-perovskites using colloidal synthesis route. To the best of our knowledge this type of structural integration between Pb-perovskites and Pb-free perovskites has not been explored until now. We demonstrated the versatility of the synthesis methodology by synthesizing numerous heterostructures with high structural tunability. It was revealed that the Pb-free double perovskites tend to grow along [110] direction, rather than the normal [100] direction observed in Pb- and Sn-based 2D perovskites. The unique growth mechanism provides insight and fundamental understanding on the crystal chemistry of this class of emerging materials. We have also demonstrated the utility of the core-shell heterostructure architecture in studying the structure-property relationship of non-emitting Pb-free perovskites using fluorescence spectroscopy by studying the anion-migration in core-shell heterostructure. We established that the metal composition in addition to organic spacer cation also plays a critical role in suppression of anion migration. $2T^+$-organic spacer cation suppressed the anion migration completely while in presence of PEA^+-organic spacer cation, we observed anion migration in hetero-halide heterostructures. Furthermore, in case of PEA^+-organic spacer cation, Ag as M^I-cation suppresses anion migration completely whereas Na as M^I-cation fails to do so, confirming the role of metal cations in suppressing the anion migration. We expect that our results and observation will be helpful in understanding the structure-property relationship in Pb-free perovskites.

Acknowledgements

This work is primarily supported by the U.S. Department of Energy, Office of Basic Energy Sciences under award number DE-SC0022082 (optical characterizations) and National Science Foundation under award number 2143568-DMR (heterostructure synthesis). AS acknowledges Science and Engineering Research Board, India for visiting doctoral fellowship (File no: SB/S9/Z-03/2017-I (2019-20)). BY and TJP acknowledge funding from the European Research Council

(ERC) under the European Union's Horizon 2020 Research and Innovation Program via Grant Agreement No. 802123-HDEM (TJP) and FWO Project G013122N "Advancing 4D STEM for atomic scale structure property correlation in 2D materials". HY acknowledges financial support from the Lillian Gilbreth Postdoc Fellowship by the college of engineering of Purdue University. The views expressed herein do not necessarily represent the views of the U.S. Department of Energy or the United States Government. A.M.K. acknowledges support from startup account F.10023800.05.002 from the Materials Engineering department at Purdue University.

Supporting Information

The supporting information file contains experimental and characterization details, density functional theory methodology, surface energy calculations, and supporting experimental results such as microscope images and XRD patterns.

Competing Financial Interests

The authors declare no competing financial interests.

References

(1) Tan, C.; Chen, J.; Wu, X.-J.; Zhang, H. Epitaxial Growth of Hybrid Nanostructures. *Nat. Rev. Mater.* **2018**, *3* (2), 17089.

(2) Huang, X.; Tan, C.; Yin, Z.; Zhang, H. 25th Anniversary Article: Hybrid Nanostructures Based on Two-Dimensional Nanomaterials. *Adv. Mater*. **2014**, *26* (14), 2185–2204.

(3) Tan, C.; Zhang, H. Epitaxial Growth of Hetero-Nanostructures Based on Ultrathin Two-Dimensional Nanosheets. *J. Am. Chem. Soc.* **2015**, *137* (38), 12162–12174.

(4) Kortan, A. R.; Hull, R.; Opila, R. L.; Bawendi, M. G.; Steigerwald, M. L.; Carroll, P. J.; Brus, L. E. Nucleation and Growth of CdSe on ZnS Quantum Crystallite Seeds, and Vice Versa, in Inverse Micelle Media. *J. Am. Chem. Soc.* **1990**, *112* (4), 1327–1332.

(5) Hoener, C. F.; Allan, K. A.; Bard, A. J.; Campion, A.; Fox, M. A.; Mallouk, T. E.; Webber, S. E.; White, J. M. Demonstration of a Shell-Core Structure in Layered CdSe-ZnSe Small Particles by X-Ray Photoelectron and Auger Spectroscopies. *J. Phys. Chem.* **1992**, *96* (9),

3812–3817.

(6) Eychmüller, A.; Mews, A.; Weller, H. A Quantum Dot Quantum Well: CdS/HgS/CdS. *Chem. Phys. Lett.* **1993**, *208* (1–2), 59–62.

(7) Milliron, D.; Hughes, S. M.; Cui, Y.; Manna, L.; Li, J.; Wang, L. W.; Alivisatos, A. P. Colloidal Nanocrystal Heterostructures with Linear and Branched Topology. *Nature* **2004**, *430* (6996), 190–195.

(8) Chen, P.; Zhang, Z.; Duan, X.; Duan, X. Chemical Synthesis of Two-Dimensional Atomic Crystals, Heterostructures and Superlattices. *Chem. Soc. Rev.* **2018**, *47* (9), 3129–3151.

(9) Zhang, Z.; Chen, P.; Duan, X. X.; Zang, K.; Luo, J.; Duan, X. X. Robust Epitaxial Growth of Two-Dimensional Heterostructures, Multiheterostructures, and Superlattices. *Science* **2017**, *357* (6353), 788–792.

(10) Zhang, Y.; Yin, L.; Chu, J.; Shifa, T. A.; Xia, J.; Wang, F.; Wen, Y.; Zhan, X.; Wang, Z.; He, J. Edge-Epitaxial Growth of 2D NbS_2-WS_2 Lateral Metal-Semiconductor Heterostructures. *Adv. Mater.* **2018**, *30* (40), 1803665.

(11) Wang, J.; Neaton, J. B.; Zheng, H.; Nagarajan, V.; Ogale, S. B.; Liu, B.; Viehland, D.; Vaithyanathan, V.; Schlom, D. G.; Waghmare, U. V.; Spaldin, N. A.,; Rabe, K. M.; Wutting, M.; Ramesh, R. Epitaxial $BiFeO_3$ Multiferroic Thin Film Heterostructures. *Science* **2003**, *299* (5613), 1719–1722.

(12) Britnell, L.; Ribeiro, R. M.; Eckmann, A.; Jalil, R.; Belle, B. D.; Mishchenko, A.; Kim, Y.-J.; Gorbachev, R. V.; Georgiou, T.; Morozov, S. V.; Grigorenko, A. N.; Geim, A. K.; Casiraghi, C.; Neto, A. H.; Novoselov, K. S. Strong Light-Matter Interactions in Heterostructures of Atomically Thin Films. *Science* **2013**, *340* (6138), 1311–1314.

(13) Ahn, C. H.; Rabe, K. M.; Triscone, J.-M. Ferroelectricity at the Nanoscale: Local Polarization in Oxide Thin Films and Heterostructures. *Science* **2004**, *303* (5657), 488–491.

(14) Gong, Y.; Lin, J.; Wang, X.; Shi, G.; Lei, S.; Lin, Z.; Zou, X.; Ye, G.; Vajtai, R.; Yakobson, B. I.; Terrones, H.; Terrones, M.; Tay, B. K.; Lou, J.; Pantelides, S. T.; Liu, Z.; Zhou, W.; Ajayan, P. M. Vertical and In-Plane Heterostructures from WS_2/MoS_2 Monolayers. *Nat. Mater.* **2014**, *13* (12), 1135–1142.

(15) Sahoo, P. K.; Memaran, S.; Xin, Y.; Balicas, L.; Gutiérrez, H. R. One-Pot Growth of Two-Dimensional Lateral Heterostructures via Sequential Edge-Epitaxy. *Nature* **2018**, *553* (7686), 63–67.

(16) Xie, S.; Tu, L.; Han, Y.; Huang, L.; Kang, K.; Lao, K. U.; Poddar, P.; Park, C.; Muller, D. A.; DiStasio, R. A.; Park, J. Coherent, Atomically Thin Transition-Metal Dichalcogenide Superlattices with Engineered Strain. *Science* **2018**, *359* (6380), 1131–1136.

(17) Min, Y.; Im, E.; Hwang, G.-T.; Kim, J.-W.; Ahn, C.-W.; Choi, J.-J.; Hahn, B.-D.; Choi, J.-H.; Yoon, W.-H.; Park, D.S.; Hyun, D, C.; Moon, G. D. Heterostructures in Two-Dimensional Colloidal Metal Chalcogenides: Synthetic Fundamentals and Applications. *Nano Res.* **2019**, *12* (8), 1750–1769.

(18) Soni, U.; Pal, A.; Singh, S.; Mittal, M.; Yadav, S.; Elangovan, R.; Sapra, S. Simultaneous Type-I/Type-II Emission from CdSe/CdS/ZnSe Nano-Heterostructures. *ACS Nano* **2014**, *8* (1), 113–123.

(19) Yadav, S.; Singh, A.; Thulasidharan, L.; Sapra, S. Surface Decides the Photoluminescence of Colloidal CdSe Nanoplatelets Based Core/Shell Heterostructures. *J. Phys. Chem. C* **2018**, *122* (1), 820–829.

(20) Singh, A.; Rohilla, J.; Hassan, M. S.; Trupthi Devaiah, C.; Ingole, P. P.; Santra, P. K.; Ghosh, D.; Sapra, S. $MoSe_2$/SnS Nanoheterostructures for Water Splitting. *ACS Appl. Nano Mater.* **2022**, *5* (3), 4293–4304.

(21) Peng, X.; Schlamp, M. C.; Kadavanich, A. V.; Alivisatos, A. P. Epitaxial Growth of Highly Luminescent CdSe/CdS Core/Shell Nanocrystals with Photostability and Electronic Accessibility. *J. Am. Chem. Soc.* **1997**, *119* (30), 7019–7029.

(22) Kagan, C. R.; Mitzi, D. B.; Dimitrakopoulos, C. D. Organic-Inorganic Hybrid Materials as Semiconducting Channels in Thin- Film Field-Effect Transistors. *Science* **1999**, *286* (5441), 945–947.

(23) Cao, D. H.; Stoumpos, C. C.; Farha, O. K.; Hupp, J. T.; Kanatzidis, M. G. 2D Homologous Perovskites as Light-Absorbing Materials for Solar Cell Applications. *J. Am. Chem. Soc.* **2015**, *137* (24), 7843–7850.

(24) Kojima, A.; Teshima, K.; Shirai, Y.; Miyasaka, T. Organometal Halide Perovskites as Visible-Light Sensitizers for Photovoltaic Cells. *J. Am. Chem. Soc.* **2009**, *131* (17), 6050–6051.

(25) Tsai, H.; Nie, W.; Blancon, J. C.; Stoumpos, C. C.; Asadpour, R.; Harutyunyan, B.; Neukirch, A. J.; Verduzco, R.; Crochet, J. J.; Tretiak, S.; Pedesseau, L.; Even, J.; Alam, M. A.; Gupta, G.; Lou, J.; Ajayan, P. M.; Bedzyk, M. J.; Kanatzidis, M. G.; Mohite, A. D. High-Efficiency Two-Dimensional Ruddlesden-Popper Perovskite Solar Cells. *Nature* **2016**, *536* (7616), 312–317.

(26) Lin, K.; Xing, J.; Quan, L. N.; de Arquer, F. P. G.; Gong, X.; Lu, J.; Xie, L.; Zhao, W.; Zhang, D.; Yan, C.; Li, W.; Liu, X.; Lu, Y.; Kirman, J.; Sargent, E. H.; Xiong, Q.; Wei, Z. Perovskite Light-Emitting Diodes with External Quantum Efficiency Exceeding 20 per Cent. *Nature* **2018**, *562* (7726), 245–248.

(27) Cho, H.; Jeong, S.-H.; Park, M.-H.; Kim, Y.-H.; Wolf, C.; Lee, C.-L.; Heo, J. H.; Sadhanala, A.; Myoung, N.; Yoo, S.; Im, S. H.; Friend, R. H.; Lee, T. W. Overcoming the Electroluminescence Efficiency Limitations of Perovskite Light-Emitting Diodes. *Science* **2015**, *350* (6265), 1222–1225.

(28) Wang, N.; Cheng, L.; Ge, R.; Zhang, S.; Miao, Y.; Zou, W.; Yi, C.; Sun, Y.; Cao, Y.; Yang, R.; Wei, Y.; Guo, Q.; Ke, Y.; Yu, M.; Jin, Y.; Liu, Y.; Ding, Q.; Di, D.; Yang, L.; Yang, L.; Xing, G.; Tian, H.; Jin, G.; Gao, F.; Friend, R. H.; Wang, J.; Huang, W. Perovskite Light-Emitting Diodes Based on Solution-Processed Self-Organized Multiple Quantum Wells. *Nat. Photonics* **2016**, *10* (11), 699–704.

(29) Yuan, M.; Quan, L. N.; Comin, R.; Walters, G.; Sabatini, R.; Voznyy, O.; Hoogland, S.; Zhao, Y.; Beauregard, E. M.; Kanjanaboos, P.; Lu, Z.; Kim, D. H.; Sargent, E. H. Perovskite Energy Funnels for Efficient Light-Emitting Diodes. *Nat. Nanotechnol.* **2016**, *11* (10), 872–877.

(30) Ha, S.-T.; Shen, C.; Zhang, J.; Xiong, Q. Laser Cooling of Organic–Inorganic Lead Halide Perovskites. *Nat. Photonics* **2016**, *10* (2), 115–121.

(31) Green, M. A.; Ho-Baillie, A.; Snaith, H. J. The Emergence of Perovskite Solar Cells. *Nat.*

Photonics **2014**, *8* (7), 506–514.

(32) Snaith, H. J. Present Status and Future Prospects of Perovskite Photovoltaics. *Nat. Mater.* **2018**, *17* (5) 372–376.

(33) Calabrese, J.; Jones, N. L.; Harlow, R. L.; Herron, N.; Thorn, D. L.; Wang, Y. Preparation and Characterization of Layered Lead Halide Compounds. *J. Am. Chem. Soc.* **1991**, *113* (6), 2328–2330.

(34) Ishihara, T.; Takahashi, J.; Goto, T. Exciton State in Two-Dimensional Perovskite Semiconductor $(C_{10}H_{21}NH_3)_2PbI_4$. *Solid State Commun.* **1989**, *69* (9), 933–936.

(35) Lee, M. M.; Teuscher, J.; Miyasaka, T.; Murakami, T. N.; Snaith, H. J. Efficient Hybrid Solar Cells Based on Meso-Superstructured Organometal Halide Perovskites. *Science* **2012**, *338* (6107), 643–647.

(36) Dou, L.; Wong, A. B.; Yu, Y.; Lai, M.; Kornienko, N.; Eaton, S. W.; Fu, A.; Bischak, C. G.; Ma, J.; Ding, T.; Ginsberg, N. S.; Wang, L. W.; Alivisatos, A. P.; Yang, P. Atomically Thin Two-Dimensional Organic-Inorganic Hybrid Perovskites. *Science* **2015**, *349* (6255), 1518–1521.

(37) Stoumpos, C. C.; Cao, D. H.; Clark, D. J.; Young, J.; Rondinelli, J. M.; Jang, J. I.; Hupp, J. T.; Kanatzidis, M. G. Ruddlesden-Popper Hybrid Lead Iodide Perovskite 2D Homologous Semiconductors. *Chem. Mater.* **2016**, *28* (8), 2852–2867.

(38) Leng, K.; Abdelwahab, I.; Verzhbitskiy, I.; Telychko, M.; Chu, L.; Fu, W.; Chi, X.; Guo, N.; Chen, Z.; Chen, Z.; Chen, Z.; Zhang, C.; Xu, Q. H.; Lu, J.; Chhowalla, M.; Eda, G.; Loh, K. P. Molecularly Thin Two-Dimensional Hybrid Perovskites with Tunable Optoelectronic Properties Due to Reversible Surface Relaxation. *Nat. Mater.* **2018**, *17* (10), 908–914.

(39) Ziffer, M. E.; Ginger, D. S. How Hybrid Perovskites Get Their Groove: Rotational Motions of Organic Cations May Screen Charge Carriers from Defects. *Science* **2016**, *353* (6306) 1365-1365.

(40) Shi, E.; Yuan, B.; Shiring, S. B.; Gao, Y.; Akriti; Guo, Y.; Su, C.; Lai, M.; Yang, P.; Kong, J.; Savoie, B. M.; Yu, Y.; Dou, L. Two-Dimensional Halide Perovskite Lateral Epitaxial

Heterostructures. *Nature* **2020**, *580* (7805), 614–620.

(41) Akriti; Shi, E.; Shiring, S. B.; Yang, J.; Atencio-Martinez, C. L.; Yuan, B.; Hu, X.; Gao, Y.; Finkenauer, B. P.; Pistone, A. J.; Yu, Y.; Liao, P.; Savoie, B. M.; Dou, L. Layer-by-Layer Anionic Diffusion in Two-Dimensional Halide Perovskite Vertical Heterostructures. *Nat. Nanotechnol.* **2021**, *16* (5), 584–591.

(42) Mathew, P. S.; DuBose, J. T.; Cho, J.; Kamat, P. V. Spacer Cations Dictate Photoinduced Phase Segregation in 2D Mixed Halide Perovskites. *ACS Energy Lett.* **2021**, *6* (7), 2499–2501.

(43) Roy, C. R.; Pan, D.; Wang, Y.; Hautzinger, M. P.; Zhao, Y.; Wright, J. C.; Zhu, Z.; Jin, S. Anion Exchange of Ruddlesden-Popper Lead Halide Perovskites Produces Stable Lateral Heterostructures. *J. Am. Chem. Soc.* **2021**, *143* (13), 5212–5221.

(44) Roy, C. R.; Zhou, Y.; Kohler, D. D.; Zhu, Z.; Wright, J. C.; Jin, S. Intrinsic Halide Immiscibility in 2D Mixed-Halide Ruddlesden-Popper Perovskites. *ACS Energy Lett.* **2022**, *7* (10), 3423–3431.

(45) Toso, S.; Gushchina, I.; Oliver, A. G.; Manna, L.; Kuno, M. Are Mixed-Halide Ruddlesden-Popper Perovskites Really Mixed? *ACS Energy Lett.* **2022**, *7* (12), 4242–4247.

(46) Mao, L.; Teicher, S. M. L.; Stoumpos, C. C.; Kennard, R. M.; DeCrescent, R. A.; Wu, G.; Schuller, J. A.; Chabinyc, M. L.; Cheetham, A. K.; Seshadri, R. Chemical and Structural Diversity of Hybrid Layered Double Perovskite Halides. *J. Am. Chem. Soc.* **2019**, *141* (48), 19099–19109.

(47) Li, X.; Traoré, B.; Kepenekian, M.; Li, L.; Stoumpos, C. C.; Guo, P.; Even, J.; Katan, C.; Kanatzidis, M. G. Bismuth/Silver-Based Two-Dimensional Iodide Double and One-Dimensional Bi Perovskites: Interplay between Structural and Electronic Dimensions. *Chem. Mater.* **2021**, *33* (15), 6206–6216.

(48) Schmitz, F.; Horn, J.; Dengo, N.; Sedykh, A. E.; Becker, J.; Maiworm, E.; Bélteky, P.; Kukovecz, Á.; Gross, S.; Lamberti, F.; Muller-Buschbaum, K.; Schlettwein, D.; Meggiolaro, D.; Righetto, M.; Gatti, T. Large Cation Engineering in Two-Dimensional Silver–Bismuth Bromide Double Perovskites. *Chem. Mater.* **2021**, *33* (12), 4688–4700.

(49) Siwach, P.; Sikarwar, P.; Rajput, S. A.; Antharjanam, S.; Chandiran, A. K. The Effect of Halogenated Spacer Cations on Structural Symmetry-Breaking in 2D Halide Double Perovskites. *Chem. Commun.* **2022**, *58* (75), 10504–10507.

(50) Xue, J.; Wang, Z.; Comstock, A.; Wang, Z.; Sung, H. H. Y.; Williams, I. D.; Sun, D.; Liu, J.; Lu, H. Chemical Control of Magnetic Ordering in Hybrid Fe–Cl Layered Double Perovskites. *Chem. Mater.* **2022**, *34* (6), 2813–2823.

(51) Pantaler, M.; Diez-Cabanes, V.; Queloz, V. I. E.; Sutanto, A.; Schouwink, P. A.; Pastore, M.; García-Benito, I.; Nazeeruddin, M. K.; Beljonne, D.; Lupascu, D. C.; Quarti, C.; Grancini, G. Revealing Weak Dimensional Confinement Effects in Excitonic Silver/Bismuth Double Perovskites. *JACS Au* **2022**, *2* (1), 136–149.

(52) Chen, M.; Dong, X.; Shan, Z.; Xu, Z.; Liu, S. F. Two-Dimensional Lead-Free Double Perovskite with Superior Stability and Optoelectronic Properties for Solar Cell Application. *J. Phys. Chem. C* **2022**, *126* (35), 14824–14831.

(53) Martín-García, B.; Spirito, D.; Biffi, G.; Artyukhin, S.; Francesco Bonaccorso; Krahne, R. Phase Transitions in Low-Dimensional Layered Double Perovskites: The Role of the Organic Moieties. *J. Phys. Chem. Lett.* **2021**, *12* (1), 280–286.

(54) Wu, G.; Liang, R.; Zhang, Z.; Ge, M.; Xing, G.; Sun, G. 2D Hybrid Halide Perovskites: Structure, Properties, and Applications in Solar Cells. *Small* **2021**, *17* (43), 2103514.

(55) Evans, H. A.; Mao, L.; Seshadri, R.; Cheetham, A. K. Layered Double Perovskites. *Annu. Rev. Mater. Res.* **2021**, *51* (1), 351–380.

(56) Yadav, P.; Gill, D.; Khurana, S.; Lamba, R. S.; Bhattacharya, S.; Sapra, S. Elucidating the Mn^{2+} Dopant Sites in Two-Dimensional Na-In Halide Perovskite. *J. Phys. Chem. C* **2022**, 2–11.

(57) Kahmann, S.; Meggiolaro, D.; Gregori, L.; Tekelenburg, E. K.; Pitaro, M.; Stranks, S. D.; De Angelis, F.; Loi, M. A. The Origin of Broad Emission in ⟨100» Two-Dimensional Perovskites: Extrinsic vs Intrinsic Processes. *ACS Energy Lett.* **2022**, *7* (12), 4232–4241.

(58) Gong, X.; Voznyy, O.; Jain, A.; Liu, W.; Sabatini, R.; Piontkowski, Z.; Walters, G.; Bappi, G.; Nokhrin, S.; Bushuyev, O.; Yuan, M.; Comin, R.; McCamant, D.; Shally, S.O.; Sargent,

E. H. Electron–Phonon Interaction in Efficient Perovskite Blue Emitters. *Nat. Mater.* **2018**, *17* (6), 550–556.

(59) Shibuya, K.; Koshimizu, M.; Nishikido, F.; Saito, H.; Kishimoto, S. Poly[Bis(Phenethyl-Ammonium) [Di-Bromido-Plumbate(II)]-Di-μ-Bromido]]. *Acta Crystallogr. Sect. E Struct. Reports Online* **2009**, *65* (11), m1323–m1324.

(60) Momma, K.; Izumi, F. VESTA : A Three-Dimensional Visualization System for Electronic and Structural Analysis. *J. Appl. Crystallogr.* **2008**, *41* (3), 653–658.

(61) Figuerola, A.; Huis, M. Van; Zanella, M.; Genovese, A.; Marras, S.; Falqui, A.; Zandbergen, H. W.; Cingolani, R.; Manna, L. Epitaxial CdSe-Au Nanocrystal Heterostructures by Thermal Annealing. *Nano Lett.* **2010**, *10* (8), 3028–3036.

(62) *X-ray Data Booklet.* https://xdb.lbl.gov/ (accesed 2023-08-09), X-Ray Properties of Elements.

(63) Savitzky, B. H.; Zeltmann, S. E.; Hughes, L. A.; Brown, H. G.; Zhao, S.; Pelz, P. M.; Pekin, T. C.; Barnard, E. S.; Donohue, J.; Rangel DaCosta, L.; et al. Py4DSTEM: A Software Package for Four-Dimensional Scanning Transmission Electron Microscopy Data Analysis. *Microsc. Microanal.* **2021**, *27* (4), 712–743.

(64) Akriti; Zhang, S.; Lin, Z.; Shi, E.; Finkenauer, B. P.; Gao, Y.; Pistone, A. J.; Ma, K.; Savoie, B. M.; Dou, L. Quantifying Anionic Diffusion in 2D Halide Perovskite Lateral Heterostructures. *Adv. Mater.* **2021**, *33* (51), 2105183.

(65) Akriti; Lin, Z.-Y.; Park, J. Y.; Yang, H.; Savoie, B. M.; Dou, L. Anion Diffusion in Two-Dimensional Halide Perovskites. *APL Mater.* **2022**, *10* (4), 040903.

(66) Mu, L.; Feng, C.; He, H. Topological Research on Molar Diamagnetic Susceptibilities for Inorganic Compounds. *Match* **2007**, *58* (3), 591–607.

Table of Contents